processes

MDPI

Article

Adsorption Characteristics and Mechanism of Methylene Blue in Water by NaOH-Modified Areca Residue Biochar

Yixin Lu [1,2], Yujie Liu [2], Chunlin Li [3], Haolin Liu [1], Huan Liu [1], Yi Tang [1], Chenghan Tang [2], Aojie Wang [2] and Chun Wang [4,*]

[1] School of Materials and Environmental Engineering, Chengdu Technological University, Chengdu 611730, China
[2] Faculty of Geosciences and Environmental Engineering, Southwest Jiaotong University, Chengdu 611756, China
[3] Sichuan Development Environmental Science and Technology Research Institute Co., Ltd., Chengdu 610094, China
[4] Sichuan Academy of Eco-Environmental Sciences, Chengdu 610046, China
* Correspondence: wangc2007@163.com; Tel.:+86-188-4831-0198

Abstract: To solve the water pollution problem caused by methylene blue (MB), areca residue biochar (ARB) was prepared by pyrolysis at 600 °C, and modified areca residue biochar (M-ARB) was obtained by modifying ARB with 1.5 mol/L NaOH, and they were utilized to adsorb and eliminate MB from water. The structural characteristics of ARB and M-ARB were examined, and the main influencing factors and adsorption mechanism of MB adsorption process were investigated. The outcomes demonstrated an increase in M-ARB's specific surface area and total pore volume of 66.67% and 79.61%, respectively, compared with ARB, and the pore structure was more abundant, and the content of oxygen element was also significantly increased. When the reaction temperature was 25 °C, starting pH of the mixture was 10, the initial MB concentration was 50 mg/L, the ARB and M-ARB dosages were 0.07 g/L and 0.04 g/L, respectively, the adsorption equilibrium was achieved at about 210 min, and the elimination rate for MB exceeded 94%. The adsorption behaviors of ARB and M-ARB on MB were more in line with the Langmuir isotherm model (R^2 > 0.95) and the quasi-secondary kinetic model (R^2 > 0.97), which was characterized by single-molecule layer chemisorption. The highest amount of MB that may theoretically be absorbed by M-ARB in water ranging from 136.81 to 152.72 mg/g was 74.99–76.59% higher than that of ARB. The adsorption process was a spontaneous heat absorption reaction driven by entropy increase, and the adsorption mechanism mainly involved electrostatic gravitational force, pore filling, hydrogen bonding, and π–π bonding, which was a complex process containing multiple mechanisms of action. NaOH modification can make the ARB have more perfect surface properties and more functional group structures that can participate in the adsorption reaction, which can be used as an advantageous adsorption material for MB removal in water.

Keywords: areca residue; methylene blue; biochar; modification; adsorption

Citation: Lu, Y.; Liu, Y.; Li, C.; Liu, H.; Liu, H.; Tang, Y.; Tang, C.; Wang, A.; Wang, C. Adsorption Characteristics and Mechanism of Methylene Blue in Water by NaOH-Modified Areca Residue Biochar. *Processes* **2022**, *10*, 2729. https://doi.org/10.3390/pr10122729

Academic Editors: Shicheng Zhang, Gang Luo, Abdul-Sattar Nizami, Andrzej Bialowiec and Yan Shi

Received: 25 November 2022
Accepted: 13 December 2022
Published: 17 December 2022

1. Introduction

Areca as a leisure food in the market that the majority of consumers love, and its market demand is increasing day-by-day. Along with the economic development and the growth of areca demand, there is also the growth of the waste areca residue produced by people after consuming areca fruits [1]. Areca residue is a solid waste contains a large amount of coarse fiber components, which lacks specialized treatment and disposal methods and is usually discarded directly in the natural environment [2]. The random disposal of areca residue not only affects environmental hygiene, but also causes different degrees of damage to the water, soil, and its surrounding environment.

A type of cationic organic dyes, called methylene blue (MB), are employed not only in textile, paper, and leather industries, but also has a large market in rubber and pharmaceutical production [3,4]. MB, as one of the most prevalent contaminants in dyeing water, is frequently detected in the natural environment [5]. The untreated MB wastewater discharged directly into the water will cause adverse effects on the aquatic ecological environment and may also directly or indirectly pose a threat to human health [6]. Therefore, the search for effective removal methods of MB in water has recently emerged as a hub for water treatment at home and abroad in recent years.

To lessen the negative impacts of MB on the aquatic environment, the effectiveness of adsorption [7], photocatalysis [8], electrocatalysis [9], nanofilms [10], and ultrasonic irradiation [11] for the treatment of MB in water has been reported extensively in the literature previously. Biochar, a new class of adsorbent emerged from adsorption method, is an environmental functional material with rich carbon content, well-developed pore structure, and high stability generated by high-temperature pyrolysis of biomass raw materials under anaerobic or oxygen-limited conditions, which shows a very broad application prospect in the field of MB treatment because of its cheap cost and numerous feedstock sources [12,13]. Common waste biomass feedstocks include plant waste [14–16], animal manure waste [17], and residual sludge [18]. Among them, the conversion of plant residues into carbon adsorbents is considered to be an economic, efficient, and environmentally friendly way to remove pollutants from wastewater. Ezz et al. [19] used rice straw digestate to prepare biochar, with a total cost of 0.3022 US $/kg and a maximum adsorption capacity of 18.90 mg/g for MB, which was a feasible economic adsorbent. Chen et al. [20] prepared biochar with rape straw residue, which can achieve the adsorption capacity of 148.94 mg/g of MB in water. Sawalha et al. [21] used eight kinds of plant biomass residues (coffee granules, almond shells, sunflower shells, pistachio shells, peanut shells, jujube seeds, jute stalks, and grape vine stalks) available locally in Palestine to prepare biochar for adsorption of MB in water and found that jute stalks provide the highest removal efficiency. The performance of biochar prepared from different types of residues varies widely. To improve the performance of biochar, a series of physical, chemical, or biological methods are usually used to modify it to have greater adsorption potential [22–26]. Among the many modification methods, alkali modification can effectively reduce the ash content of biochar, change the elemental composition, functional group distribution, specific surface area, and pore structure of biochar surface [27]. Thus, it becomes a promising modification pathway. Areca residue is a waste biomass that contains a lot of organic material and can be processed to yield biochar. However, the conventional treatment of areca residue is still mainly to treat it as solid waste, and there are few reports on the exploration of making it into biochar or modified biochar. What is more, the research on the application of modified areca residue biochar in the removal of MB from wastewater are even less, and its adsorption feasibility and mechanisms are still unclear.

Therefore, in this study, waste areca residue was selected for the preparation of biochar, and NaOH was used as a modifier to modify them and investigate their feasibility for application in the removal of MB from water. The primary goals of this research were (1) to look into how NaOH modification affects the structural features of areca residue biochar; (2) to investigate the factors influencing the adsorption effect of areca residue biochar on MB before and after NaOH modification; and (3) to resolve the kinetics, isotherms, thermodynamic characteristics, and adsorption mechanism of the adsorption process, as well as to address the issue of waste areca residue pollution, while also reusing it to treat MB in water, and realize the reuse of waste biomass.

2. Materials and Methods

2.1. Reagents and Raw Materials

The areca residue was gathered in the streets of Zhuzhou City, Hunan Province, China, from an areca residue collection column, a portable device specifically designed to collect areca residue discarded by the public. After removing the impurities from the waste areca

residue and drying it, the residue was crushed by a crusher. After being crushed, the powdered areca residue was sieved using a 60 mesh sieve to remove any particles larger than 0.25 mm before being used as a raw material for the subsequent preparation of biochar.

The main chemical reagents used in the experiments included analytically pure MB ($C_{16}H_{18}ClN_3S$), hydrochloric acid (HCl), caustic soda (NaOH), and ethanol (C_2H_5OH), which was purchased from Chengdu Kelong Chemical Reagent Factory, and $C_{16}H_{18}ClN_3S$ was used to prepare the MB solution. The water used in the experiment for solution preparation, sample analysis, and vessel rinsing referred to deionized water, unless otherwise specified.

2.2. Preparation and Modification of Biochar

After drying, the powdered areca residue was packed in a quartz boat, put into the chamber of a tube furnace, warmed to 600 °C with a 20 °C/min temperature gradient, and then set 150 min at a steady temperature. The quartz boat was chilled to room temperature after the pyrolysis. Then, the item was split into two sections. The pH of the supernatant was stabilized by washing one portion of the pyrolysis product with deionized water, dried, and sieved through a 100-mesh sieve to obtain a sieve out product with particle size less than 0.15 mm, which was areca residue biochar labeled as ARB and stored for backup. Another part of the pyrolysis product was modified with NaOH solution at 1.5 mol/L. The following was the course of treatment: 50 mL NaOH solution was added to each 1 g of pyrolysis product, and the product was shaken at a frequency of 150 rpm one day at 25 °C. The residue was sorted out and repeatedly rinsed with deionized water to stabilize the supernatant's pH, dried and sieved through 100-mesh sieve to obtain a sieve product with particles size of no more than than 0.15 mm, which was the modified areca residue biochar labeled as M-ARB and kept as a reserve.

2.3. Characterization of Biochar

The structures of ARB and M-ARB were characterized using BET, SEM-EDS, and FTIR techniques to analyze their basic physicochemical properties. Among them, the total pore volume, average pore size, and specific surface area of ARB and M-ARB were analyzed by NOVA 4000e-type specific surface area analyzer (Quantachrome, Beijing, China). The surface morphology was examined by Gemini 300 field emission scanning electron microscope (ZEISS, Oberkochen, Germany), and the EDS (line scan) was analyzed by Xplore energy spectrometer (OXFORD, Oxfordshire , UK). Surface functional groups were analyzed by a Nicolet 670 FTIR spectrometer (Thermo Fisher, Waltham, MA, USA).

2.4. Sequential Batch Adsorption Experiments

In a batch of 250 mL conical flasks, 100 mL of MB solution and an appropriate amount of biochar were added to each batch, and the sequential batch tests were run at various initial pH of the solutions (2–11), biochar dosing amounts (0.02–0.11 g), contact times (30–400 min), and initial MB concentrations (40–150 mg/L), in order to study the effects of ARB and M-ARB on the adsorption of MB. The main factors influencing the adsorption of ARB and M-ARB were investigated. By adding 1 mol/L of HCl and NaOH, the solution's original pH was changed. To investigate the effect of biochar dosing, the pH, reaction time, and starting MB concentration were set to 10, 400 min, and 50 mg/L, respectively. To study the influence of reaction time, the initial pH, ARB dosing, M-ARB dosing, and initial MB concentration were set to 10, 0.07 g, 0.04 g, and 50 mg/L, respectively. To exam the impact of the starting MB concentration, the pH, ARB dosage, M-ARB dosage, and contact time were set to 10, 0.07 g, 0.04 g, and 400 min, respectively. Experiments were conducted in a THZ-82 air-bath thermostat shaker (Changzhou Yineng Experimental Instrument Factory, Changzhou, China) with the oscillation frequency set to 150 rpm and the temperature set to 25 °C.

After the shaking, the mixture was put into a 2–16P centrifuge (SIGMA, Osterode, Germany) and spun for five minutes at 4000 rpm. After centrifugation, the supernatant

was loaded into a cuvette, and the remaining MB concentration was tested by a 722S visible spectrophotometer (Shanghai Jingke, Shanghai, China) at 665 nm. Equations (1) and (2) were used to calculate the adsorption amount (q_t, mg/g) and removal rate (w, %) of MB, respectively.

$$w = \frac{\rho_0 - \rho_t}{\rho_0} \times 100\% \quad (1)$$

$$q_t = \frac{(\rho_0 - \rho_t)V}{m} \quad (2)$$

where ρ_0 refers to the MB starting mass concentration in solution, mg/L; ρ_t refers to the MB mass concentration at moment t, mg/L; V refers to the water sample volume, mL; m refers to the dosage of ARB and M-ARB, g.

During the analysis of regeneration performance, ethanol was used as the desorption agent. ARB and M-ARB saturated with MB were added to ethanol, respectively, and the constant temperature oscillation was conducted for 90 min at 25 °C and 150 r/min. After the oscillation, the filter residue was washed with deionized water three times. After drying the filter residue, the removal rates of MB by ARB and M-ARB after desorption were tested. The same batch of ARB and M-ARB was repeatedly operated five times to investigate the changes in the adsorption properties of ARB and M-ARB.

2.5. Adsorption Kinetics

In order to better understand the kinetics of adsorption behavior of MB on ARB and M-ARB, the experimental data of the adsorption amount at different adsorption times were selected and fitted with the quasi-primary kinetic model, quasi-secondary kinetic model, Elovich model, and Weber–Morris model, as shown in Equations (3), (4), (5), and (6), respectively.

i. Quasi-primary kinetic model

$$\ln(q_e - q_t) = \ln q_e - k_1 t \quad (3)$$

ii. Quasi-secondary dynamical model

$$\frac{t}{q_t} = \frac{t}{q_e} + \frac{1}{k_2 q_e^2} \quad (4)$$

iii. Elovich model

$$q_t = k_3 \ln t + a \quad (5)$$

iv. Weber–Morris model

$$q_t = k_{4i} t^{0.5} + b_i \quad (6)$$

where the MB adsorption at equilibrium and at time t are represented by q_e and q_t , respectively, mg/g; t is the contact time, min. k_1 is the quasi-primary kinetic model's rate constant, min^{-1}; k_2 is the quasi-secondary kinetic model's rate constant, g/(mg × min); k_3 is the Elovich model's rate constant, mg/(g × min); k_{4i} is the Weber–Morris model rate constant, mg/(g × $min^{0.5}$); © is the i-th stage of adsorption; a and b_i are the empirical constants of the Elovich and Weber–Morris models, respectively.

2.6. Adsorption Isotherm

To investigate the relationship between MB concentration and MB adsorption at adsorption equilibrium, the experimental data of MB adsorption at reaction temperatures of 25–45 °C and initial MB concentrations of 40–150 mg/L were selected and fitted with the Langmuir model, Freundlich model, and Temkin model, given by Equations (7), (8), and (9), respectively.

i. Langmuir model.

$$q_e = \frac{q_m K_L \rho_e}{1 + K_L \rho_e} \quad (7)$$

ii. Freundlich model.

$$q_e = K_F \rho_e^{1/n} \quad (8)$$

iii. Temkin model.

$$q_e = K_T \ln \rho_e + c \quad (9)$$

where q_e and q_m are the equilibrium adsorption and theoretical maximum adsorption of MB, respectively, mg/g; ρ_e refers the MB mass concentration at adsorption equilibrium, mg/L; K_L is the Langmuir constant, L/mg; k_F and n are the correlation constants of the Freundlich model; K_T and c are the correlation constants of the Temkin model.

2.7. Adsorption Thermodynamics

A thermodynamic model, as shown in Equations (10) and (11), was used to make the experimental results more suitable for the adsorption of MB in water by ARB and M-ARB at different reaction temperatures to analyze the thermodynamic characteristics of the adsorption process.

$$\Delta G^\theta = -RT \ln \frac{q_e}{\rho_e} \quad (10)$$

$$\ln \frac{q_e}{\rho_e} = -\frac{\Delta H^\theta}{RT} + \frac{\Delta S^\theta}{R} \quad (11)$$

where ΔG^θ refers the Gibbs free energy change, kJ/mol; R refers the ideal gas constant, 8.314 J/(mol × K); T refers the thermodynamic temperature, K; q_e refers the equilibrium adsorption amount of MB, mg/g; ρ_e refers the mass concentration of MB at adsorption equilibrium, mg/L; ΔH_θ refers the enthalpy change, kJ/mol; ΔS^θ is the entropy change, kJ/(mol × K).

3. Results and Discussion

3.1. Structural Characterization of ARB

Table 1 reflects the results regarding the BET analysis of ARB and M-ARB. It demonstrates that, as compared to ARB, M-ARB's specific surface area and total pore volume increased, but the average pore size decreased, which meant the pore structure of areca residue biochar could be altered by NaOH modification. The specific surface area of M-ARB reached 105 m^2/g, which increased by 66.67%, compared with ARB. The total pore volume of M-ARB increased by 79.61%, compared with ARB and reached 0.282 cm^3/g, while the average pore size decreased by 38.92%, compared with ARB. Mu et al. [28] prepared tea residue biochar (TRB) by NaOH-assisted pyrolysis, and compared to unmodified TRB, its specific surface area and total pore volume lessened by 59.64% and 24.77%, while the average pore size increased by 85.35%, contrary to the change pattern obtained in this study. This may be because the specific surface area and total pore volume of TRB decreased because of the inhibition of biomass pyrolysis by the addition of NaOH during the pyrolysis process in this study. In contrast, in this study, NaOH was used to modify the products after pyrolysis, and during the modification process, NaOH was in full contact with the areca residue biochar and chemically reacted with the impurities produced by the thermal decomposition of the biochar, which led to the solubilization of the pores, causing more pore structures and bringing about the pores' enlargement. The investigation by Choudhary et al. [29] confirmed a related occurrence using NaOH impregnation to treat *Opuntia ficus-indica* biochar. The increase in the specific surface area and total pore volume of

M-ARB can give more adsorption places for the attachment of more places for contaminants to attach themselves to adsorb, which makes the adsorption potential of M-ARB better than that of ARB. Zhou et al. [30] prepared nitrogen-doped biochar nanomaterials for the adsorption of cationic dyes from seaweed at 600 °C pyrolysis temperature and found that a greater specific surface area and appropriate pore structure can minimize the resistance to the diffusion process of pollutants to biochar and provide more active adsorption sites, which was beneficial for improving the adsorption capacity of organic dyes.

Table 1. Results of BET analysis of ARB and M-ARB.

Biochar	Specific Surface Area (m^2/g)	Total Hole Volume (cm^3/g)	Average Pore Size (nm)
ARB	63	0.157	5.593
M-ARB	105	0.282	3.416

The SEM analysis results of ARB and M-ARB can be seen in Figure 1. As can be observed, ARB's surface was comparatively smooth, and the pore structure was not immediately apparent. Compared with ARB, the porosity of M-ARB was significantly higher, the diameter of pores was reduced, the pores were more densely arranged, and the surface was more concave and uneven, showing a honeycomb shape. The analysis suggested that, during the pyrolysis process, water, organic matter, and other volatile substances inside the areca residue were released, which prompted the formation of pore structure. However, some substances were not volatile, and their blockage inside the biochar or attachment to the biochar surface resulted in the insufficient opening of pores [31]. The etching effect of NaOH cleared the impurities attached to the biochar surface and blocked inside the biochar, which led to the formation of more pore structures. The etching pore-making effect of NaOH led to the appearance of more microporous structures in the biochar, which can provide more subsequent pollutant adsorption. The pore-forming effect of NaOH made biochar appear to have more microporous structures, which can provide more adsorption sites and larger adsorption space for subsequent pollutant adsorption [32].

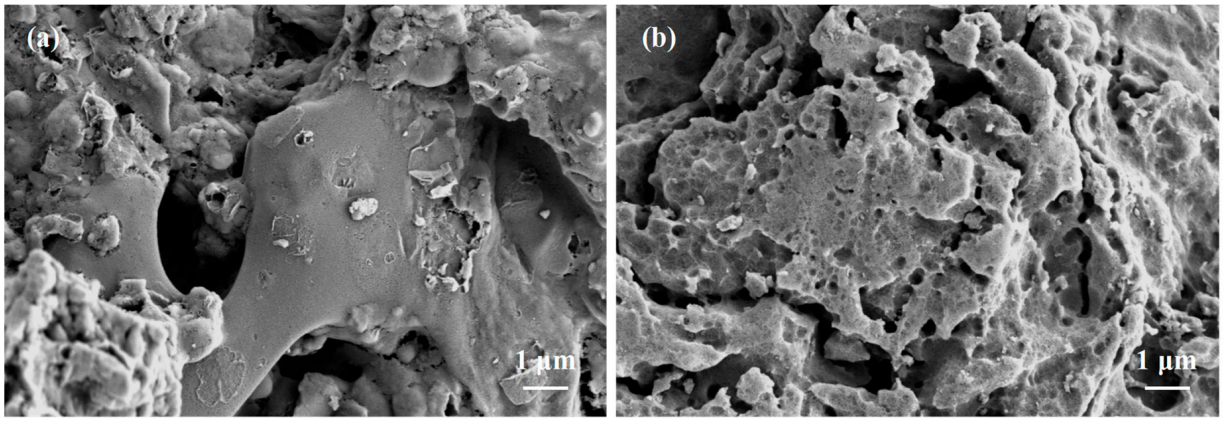

Figure 1. Scanning electron microscope of ARB (**a**) and M-ARB (**b**).

To understand the elemental composition of ARB and M-ARB, they were analyzed by EDS, and the results can be seen in Figure 2. Figure 2 shows that the areca residue biochar prepared by pyrolysis was very rich in elemental species. The highest atomic mass fraction (*At*) of C element was 88.59% in ARB and 79.32% in M-ARB, indicating that both had a more stable aromatic carbon structure. However, the elemental C content in the modified ARB was reduced, compared with the unmodified ARB, which may be due to two reasons. One is that the NaOH modification makes some of the C elements react with it and be carried out with the dissolution of other substances, resulting in the reduction of C content [33]; the other is that the NaOH modification makes the content of other elements

increase, which indirectly results in the relative reduction of C elements in M-ARB [34]. Compared with ARB, the atomic mass fraction of O element in M-ARB showed the most significant increase by 4.89 percentage points, and the content of elements N, Na, Mg, Al, S, Cl, and Ca also increased. NaOH modification exposed the oxygen-containing functional groups masked by areca residue biochar, and more types of elements formed chemical bonds with or attached to the biochar, which was more conducive to the adsorption of pollutants. In a study by Cai et al. [35] on the modification of Oiltea camellia shells biochar with NaOH, it was also found that the alkali modification improved the functional group structure on biochar surface, added the number of oxygen-containing functional groups, and consequently significantly improved its ability to absorb and remove contaminants.

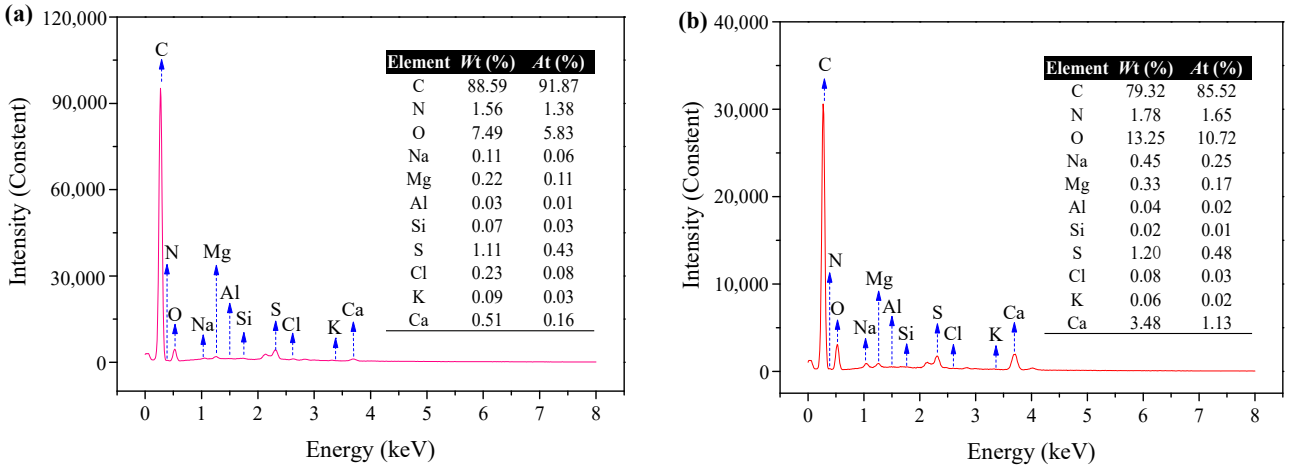

Figure 2. EDS analysis results of ARB (**a**) and M-ARB (**b**).

3.2. Analysis of Adsorption Influencing Factors

3.2.1. Effect of Initial pH of the Solution

The effect of the initial pH upon the effect of ARB and M-ARB on the adsorption of MB can be seen in Figure 3. The adsorption and removal rate of MB by ARB and M-ARB increased rapidly in the interval of pH range from 2 to 4. In the interval of the pH range from 4 to 8, the increasing trend of the MB removal effect became slower. In the interval of pH range from 8 to 10, the increasing rate of MB removal became fast again, but showed a decreasing trend after the pH exceeded 10. When the solution's original pH was 10, the adsorption value of MB by ARB and M-ARB were 86.23 mg/g and 120.05 mg/g, respectively, reaching the maximum adsorption value at this pH condition, while the adsorption of M-ARB was significantly higher than that of ARB, and its corresponding MB removal rate was increased by 27.06%, compared with that of ARB. This showed that the alkaline water environment was more favorable for the adsorption of MB by areca residue biochar, and the optimal solution initial pH was 10.

It was analyzed that, under acidic conditions, the higher concentration of hydrogen ions in water not only competed with MB cations for adsorption, but also caused electrostatic repulsion between the surface of biochar and MB cations, due to protonation; thus, the more acidic the conditions, the less effective the MB removal [36]. As the starting pH added, this competitive adsorption and electrostatic repulsion gradually decreased; thus, the adsorption effect of ARB and M-ARB on MB gradually picked up with the increase of pH [37]. However, after pH exceeded 10, the presence of too many anions in water increased the attraction for MB, resulting in MB that is not easily diffused from the liquid phase to biochar surface; thus, the removal of MB began to deteriorate. In examining the pH impact from 2.5 to 11 on the removal of MB by rice husk, cow dung, and sludge biochar, Ahmad et al. [38] found that the adsorption behavior depended mainly upon the electrostatic gravitational force between biochar and MB. MB existed in cationic form in aqueous solution, and higher pH biochar particles accumulated more negative charges on

the surface, thus promoting the adsorption of MB through electrostatic gravitational force, while lower pH slowed down the efficiency of adsorption occurrence.

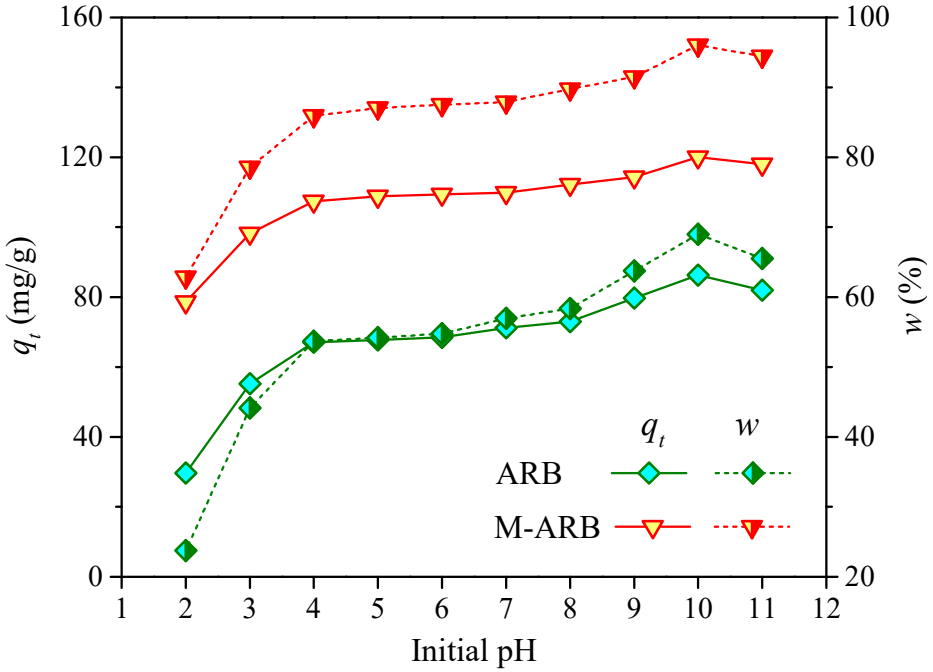

Figure 3. Effect of initial pH on MB adsorption performance.

3.2.2. Effect of Biochar Dosage

The amount of biochar added is the most direct factor for determining the adsorption effect, which determines the number of adsorption sites available for pollutant removal and the size of the adsorption capacity. Generally, the higher the amount of biochar added, the better the adsorption effect, but in practice, all factors should be integrated to select an optimal amount to achieve the best adsorption efficiency, while avoiding the waste of resources [39].

The impacts of diverse ARB and M-ARB dosing amounts on the removal efficiency and adsorption of MB in water were investigated, and the outcomes can be seen in Figure 4. As depicted in Figure 4, the adsorption of MB through ARB and M-ARB showed a rapid decreasing trend when the dosing amount raised to 0.6 g/L from 0.2 g/L, and this trend gradually slowed down after the dosing amount exceeded 0.6 g/L. The removal rates of MB by ARB increased rapidly when the dosage of ARB raised from 0.2 g/L to 0.7 g/L and then slowed down after the dosage of ARB exceeded 0.7 g/L. The removal efficiency of MB by M-ARB increased rapidly when the dosage of M-ARB raised from 0.2 g/L to 0.4 g/L and then slowed down after the M-ARB dosage exceeded 0.4 g/L. It was analyzed that, when the MB starting concentration was certain, with the increase of biochar dosing, the adsorption sites on biochar increased, the total adsorption capacity raised, and the MB clearance rate was higher because more MB might be adsorbed [40]. However, the utilization rate of biochar per unit mass decreased; thus, the MB adsorption capacity decreased [41]. Considering both adsorbent utilization and adsorbate removal, 0.07 g/L was selected as the ideal amount of ARB to take, and the adsorption amount and clearance rate of MB at this dosage were 68.37 mg/g and 95.72%, respectively. In contrast, the optimum dosage of M-ARB was only 0.04 g/L. The adsorption amount and removal rate of MB reached 120.08 mg/g and 96.06%, respectively, at this dosage. It can be seen that, compared with ARB, M-ARB can obtain better MB treatment effect with less dosage.

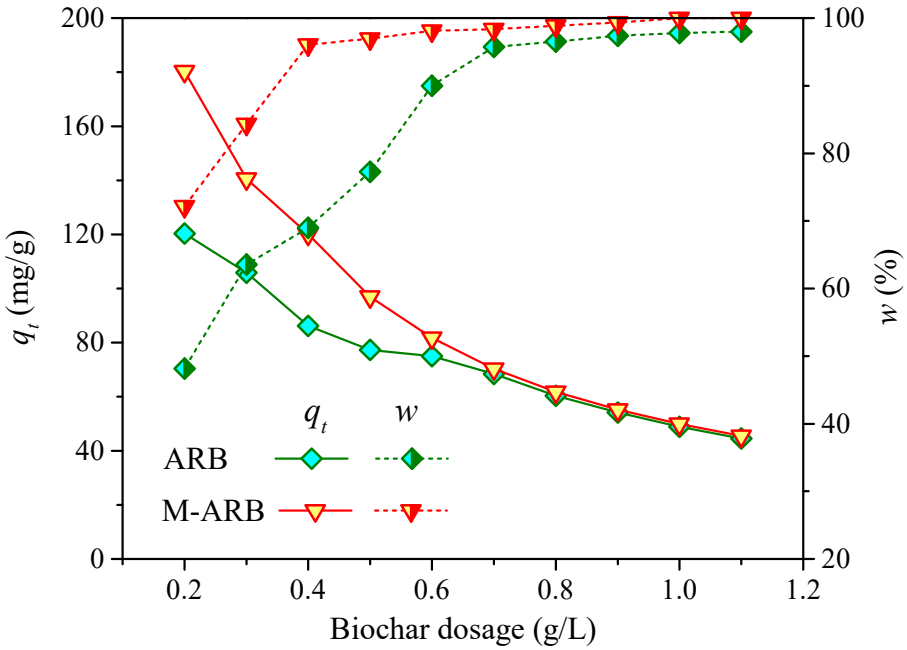

Figure 4. Effect of biochar dosage on MB adsorption performance.

3.2.3. Effect of Contact Time

Adsorption is a dynamic equilibrium process, and when pollutants are adsorbed, they need a certain amount of time to reach adsorption equilibrium; insufficient contact time may lead to incomplete adsorption, and too long contact time may lead to desorption and also waste time [42]. For this reason, this study investigated the adsorption and removal of MB from water by ARB and M-ARB at different contact times, and the results can be seen in Figure 5.

It is evident that, as the reaction time increased, both the adsorption amount and removal efficiency of MB exhibited an upward trend, and this trend, in turn, showed a pattern of fast, then slow, and finally, stable [43]. The rate of adsorption and elimination during the 30–120 min reaction time of MB by these two types of biochar showed a rapid increasing trend and belonged to the rapid adsorption stage (Stage I). At a contact time of 120–210 min, the rising trend became slower and belonged to the slow adsorption stage (Stage II). At a contact time of 210–400 min, the rising trend was very slow, and the overall trend remained the same, which belonged to the equilibrium adsorption stage (Stage III). Stage I was the initial step of the reaction, and the MB concentration in this stage was high. A lot of free adsorption places can be seen on the ARB and M-ARB's surface, and the difference of MB concentration between solid and liquid phases was large, so the driving force for MB to approach ARB and M-ARB was large, and MB can be rapidly adsorbed by ARB and M-ARB in a short period of time. After entering Stage II, the concentration of MB decreased little-by-little, and the available adsorption points on the ARB and M-ARB gradually reduced, too. The concentration difference of MB between the solid and liquid interface decreased, and the driving force for adsorption decreased, so the rate of MB adsorption by ARB and M-ARB became slower. After entering Stage III, the MB concentration decreased to a very low level, and the adsorption sites on the ARB were gradually occupied until saturation was reached and the MB removal effect was maximized. Therefore, the adsorption could reach equilibrium when the contact time was about 210 min. At this time, the adsorption amount and removal rate of MB by ARB were 67.21 mg/g and 94.10%, and those of MB by M-ARB were 118.28 mg/g and 94.62%, respectively. Overall, the NaOH modification could make the areca residue biochar possess a better MB removal effect in a shorter time.

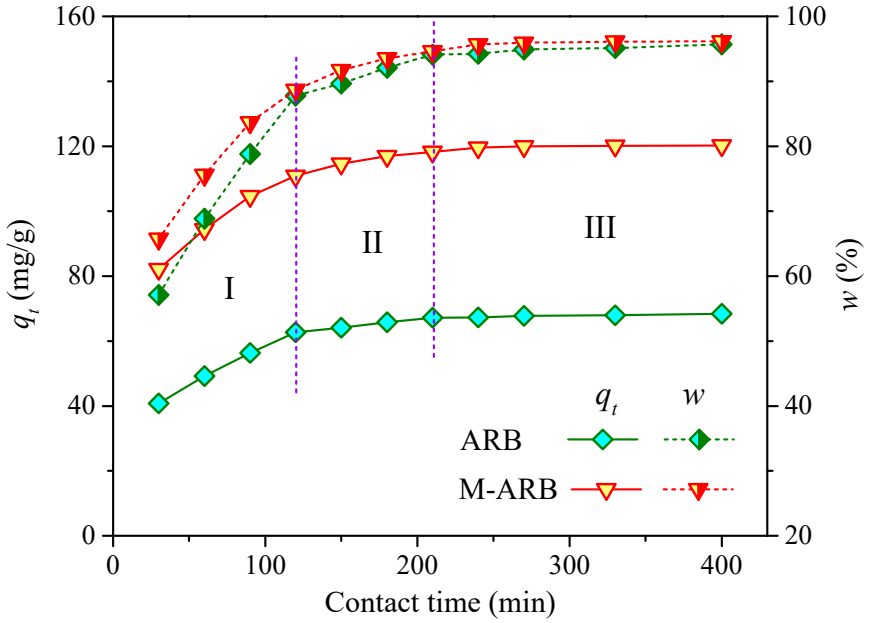

Figure 5. Effect of contact time on MB adsorption performance.

3.2.4. Effect of MB Initial Concentration

The starting concentration of adsorbent is also a vital element in the adsorption behavior. If the initial concentration of adsorbent is too low, the biochar cannot be fully utilized. Too high an initial concentration of adsorbent tends to exceed the adsorption capacity range of biochar [44]. The results of the investigation into the impact of various starting MB concentrations on the adsorption effect of ARB and M-ARB are displayed in Figure 6.

It can be seen that, at the starting MB concentration of 40 mg/L, the adsorption amounts of ARB and M-ARB on MB were 55.53 mg/g and 97.68 mg/g, respectively, and MB was removed at a rate of above 97%. At a 150 mg/L starting MB concentration, the adsorption amounts of ARB and M-ARB to MB increased to 77.33 mg/g and 135.33 mg/g, respectively, but the removal rate of MB decreased to less than 40%. When the initial concentration of MB raised from 40 mg/L to 150 mg/L, the elimination rate of MB by ARB and M-ARB kept decreasing. The adsorption amount increased rapidly at the initial MB concentration of 40–60 mg/L, and then the increase gradually decreased. The analysis suggested that ARB and M-ARB could provide sufficient adsorption sites when the initial MB concentration was low, and thus, efficient MB removal could be achieved. However, due to the low initial concentration of MB, there was still a large amount of unused residual space on the ARB and M-ARB, leading to a low adsorption efficiency of MB per unit mass of ARB and M-ARB. At a fixed amount of ARB and M-ARB dosing, as the initial MB concentration increased, the MB concentration difference between the solid–liquid phases increased, the adsorption driving force was enhanced, and the ARB and M-ARB was more fully utilized, thus the adsorption capacity per unit mass of ARB and M-ARB increased [45]. However, with the initial MB concentration rising even higher, the sites available for adsorption on the ARB and M-ARB were insufficient or had reached saturation, resulting in a decrease of the MB removal rate and more MB remaining in the water that cannot be effectively adsorbed. Thus, it is evident that there was a high removal rate, but the adsorption capacity was low when the initial MB concentration was too low, and the adsorption capacity was high, but the removal rate was low when the initial MB concentration was too high. Therefore, the optimum initial concentration of MB that can be treated with the given amount of biochar was 50 mg/L. Under this condition, the adsorption amounts of ARB and M-ARB for MB were 68.37 mg/g and 120.23 mg/g, respectively, and the elimination rates of MB were 95.72% and 96.18%, respectively.

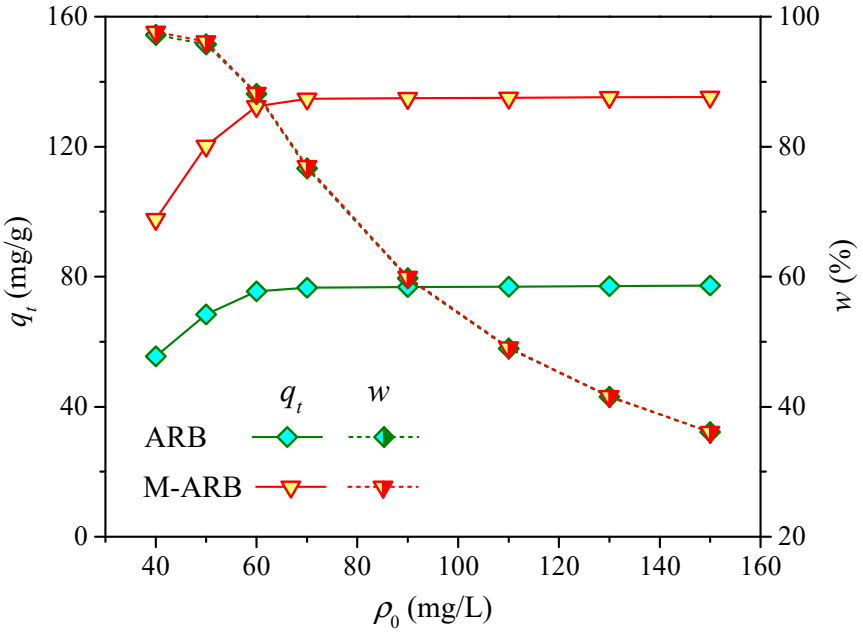

Figure 6. Effect of initial MB concentration on its adsorption performance.

3.3. Adsorption Kinetics

The results of the kinetic fitting for the MB adsorption process on ARB and M-ARB are shown in Figure 7, and the fitted factors can be seen in Table 2. The correlation coefficient R^2 obtained after fitting the adsorption data can be seen using the quasi-secondary kinetic model and exceeded 0.97, which was higher than the quasi-primary kinetic model and the Elovich model. This showed that the adsorption behavior of MB by ARB and M-ARB owned greater conformity to the quasi-secondary kinetic model, reflecting that chemisorption mainly occurred in the removal of MB by these two areca residue biochar [46]. According to the fitted parameters of the quasi-secondary kinetic model, the equilibrium adsorption capacity of M-ARB for MB was 127.23 mg/g and the rate constant k_2 was 0.0005 g/(mg × min), both of which were higher than that of ARB, indicating that the modified areca residue biochar had better adsorption performance for MB.

Table 2. Adsorption kinetics fitting parameters of MB onto ARB and M-ARB.

Model	Parameter	ARB	M-ARB
Quasi-primary kinetic	q_e (mg/g)	66.90	117.22
	k_1 (min^{-1})	0.0249	0.0329
	R^2	0.9220	0.8497
Quasi-secondary kinetic	q_e (mg/g)	74.33	127.23
	k_2 [g/(mg × min)]	0.0004	0.0005
	R^2	0.9761	0.9793
Elovich	a	35.17	74.49
	k_3 [mg/(g × min)]	6.6396	9.1936
	R^2	0.8653	0.8761

To examine the rate-controlling steps of MB adsorption in water by ARB and M-ARB, the segments of the adsorption experiment data were fitted with the Weber–Morris model, and the results are given in Figure 8, along with the fitted parameters for each phase in Table 3. Figure 8 and Table 3 show that the Weber–Morris model may be used to fit the adsorption data into three stages. The correlation coefficient R^2 of the fit for stage I (30–120 min) was the highest, reaching over 0.99, which was higher than that of stage II (120–210 min) and stage III (210–400 min). It is evident that the early stage of adsorption was more consistent with the characteristics of the Weber–Morris model. In terms of the

magnitude of the rate constant k_4 values of the Weber–Morris model, stage I had the highest k_4 value, indicating that adsorption can occur rapidly at this stage. The gradually decreasing k_4 values for stages II and III indicated that the adsorption rate gradually became slower, and MB started to travel through the internal pores of biochar and searched for adsorption sites, but the adsorption gradually moved toward saturation as the external driving force decreased and the internal diffusion resistance increased [47]. The results of this analysis were consistent with the previous inferences made when it came to the impact of reaction time upon the adsorption effect of MB. The rate constant k_4 for MB adsorption of M-ARB were 1.33 and 1.16 times higher than those of ARB in stages I and II, respectively, indicating that the MB adsorption process on M-ARB was more likely to reach equilibrium than on ARB. It was also because of this that the remaining MB content in the aqueous solution available for M-ARB adsorption was very small after entering stage III; thus, the rate constant k_4 values for this stage decreased dramatically. A similar three-stage pattern of adsorption and decreasing rate constants for adsorption was also found in the research by Qing et al. upon the adsorption of phosphate in water by sodium alginate/zirconium hydrogels [48]. Moreover, none of the three fitted lines crossed the origin of the coordinate axis, indicating that the ARB and M-ARB adsorption MB process's rate-controlling steps involved other mechanisms besides intraparticle diffusion, which was also controlled by a combination of other factors, such as liquid film diffusion and adsorption reaction [48,49].

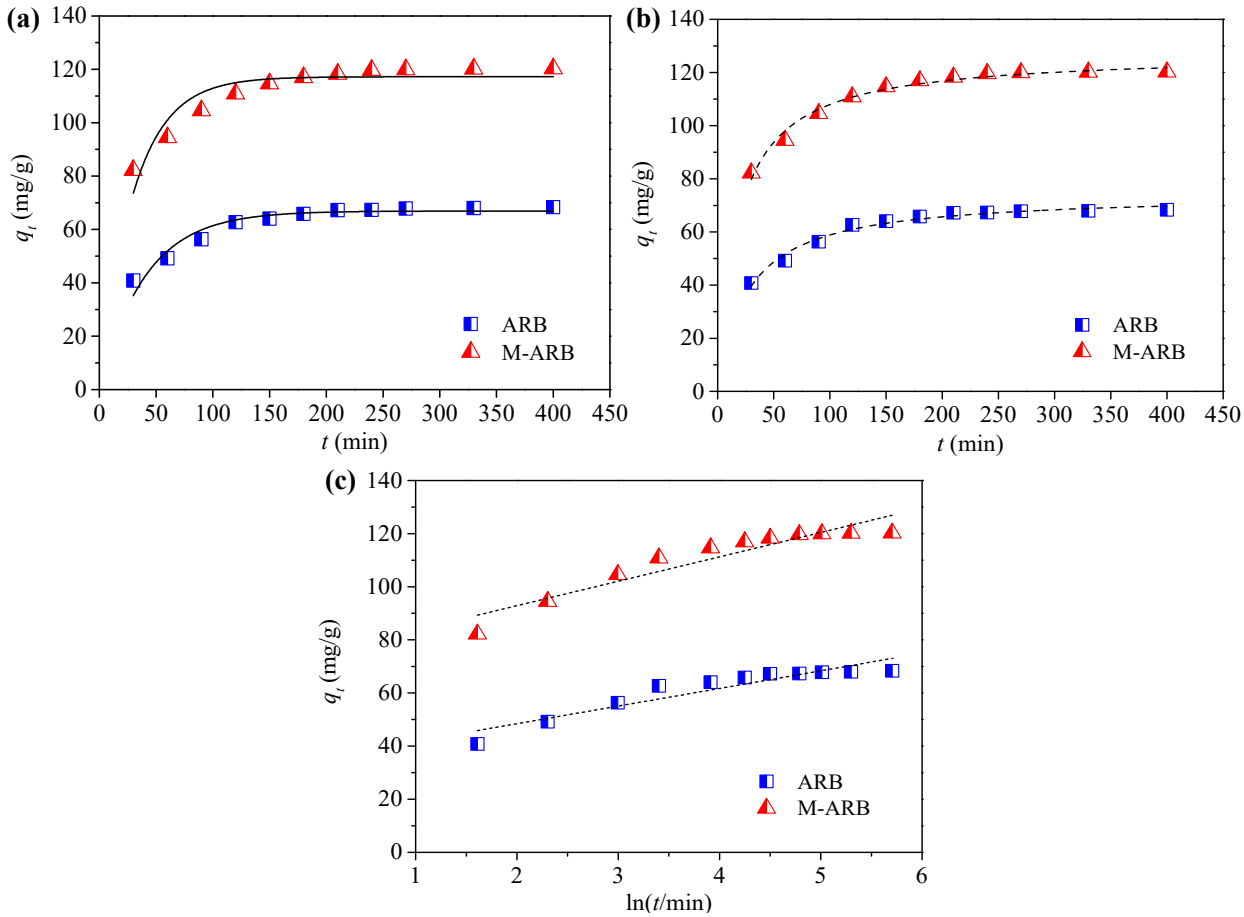

Figure 7. Adsorption kinetics fitting of MB onto ARB and M-ARB: (**a**) quasi-primary kinetic model, (**b**) quasi-secondary kinetic model, and (**c**) Elovich model.

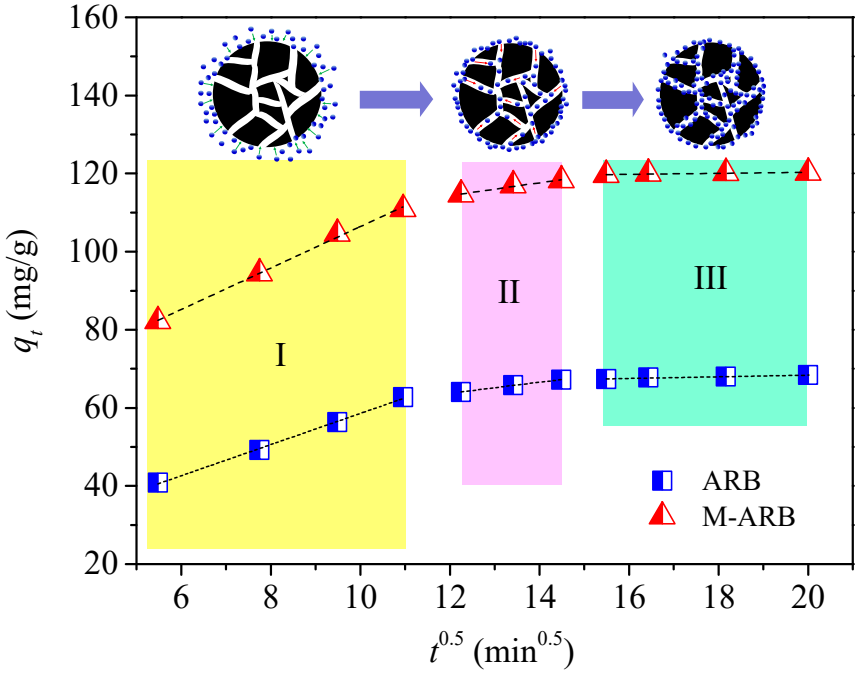

Figure 8. Segmented fit of the Weber–Morris model.

Table 3. Segmented fit parameters of the Weber–Morris model.

Stage	Parameter	ARB	M-ARB
I	b_1	18.65	53.33
	k_{41} (mg/(g × min$^{0.5}$))	3.9917	5.3098
	R^2	0.9979	0.9961
II	b_2	46.84	94.77
	k_{42} (mg/(g × min$^{0.5}$))	1.4079	1.6319
	R^2	0.9981	0.9649
III	b_3	64.19	117.77
	k_{43} (mg/(g × min$^{0.5}$))	0.2093	0.1261
	R^2	0.8924	0.8002

3.4. Adsorption Isotherm

The isothermal adsorption fitted consequences of MB by ARB and M-ARB are shown in Figure 9, and their fitted parameters can be seen in Table 4. From the fitted parameters of the three isothermal adsorption models, the adsorption procedure can be found to be more compatible with the Langmuir model, and its fitted correlation coefficient R^2 was 0.9574–0.9895, which was greater than that of the Freundlich and Temkin models by a large margin. Therefore, the adsorption of ARB and M-ARB on MB was dominated by monolayer molecular adsorption, and there was microporous filling during the adsorption process, and the limit adsorption amount was the filling amount of microporous [50]. According to the Langmuir model fitting parameters, the theoretical maximum adsorption of M-ARB on MB was 136.81–152.72 mg/g, which was 74.99–76.59% higher than that of ARB. The values of the Langmuir constant K_L for M-ARB ranged from 2.9839 to 6.7535, which was 20.06% to 48.81% higher than that of ARB. As seen, the biochar made from modified areca residue displayed increased adsorption ability and can be employed as a more effective adsorbent to remove of MB in water. Additionally showing that heat might encourage the occurrence of adsorption, the values of q_m and K_L rose with the rise in reaction temperature, which led to a more complete removal of MB from aqueous solution [51].

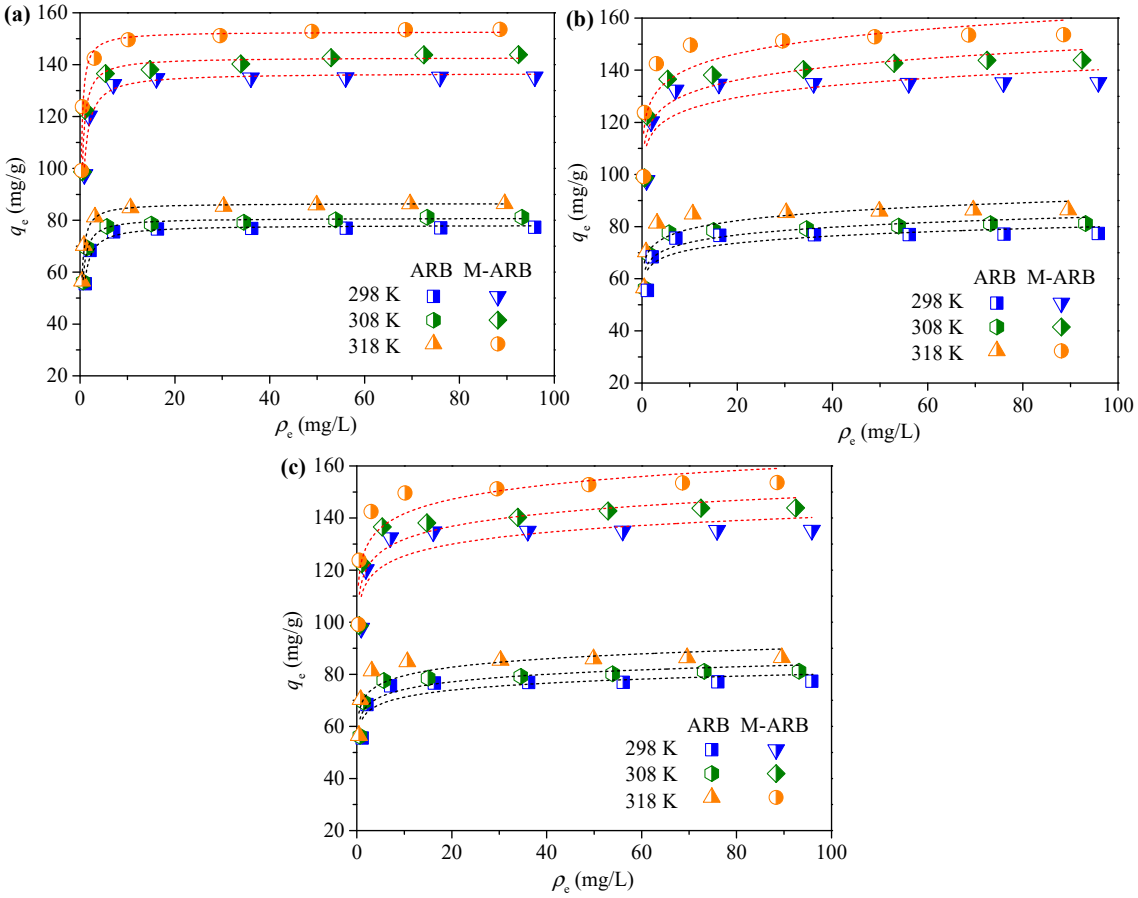

Figure 9. Isothermal adsorption fitting of Langmuir model (**a**), Freundlich model (**b**), and Temkin model (**c**).

Table 4. Isothermal adsorption fitting parameters of MB onto ARB and M-ARB.

Biochar	*T*/K	Langmuir Model			Freundlich Model			Temkin Model		
		q_m	K_L	R^2	1/*n*	K_F	R^2	*c*	K_T	R^2
ARB	298	78.18	2.4854	0.9574	0.0522	63.0093	0.6350	62.32	3.8667	0.6636
	308	80.87	3.6369	0.9881	0.0549	65.1281	0.7405	64.63	4.1659	0.7695
	318	86.56	4.5384	0.9895	0.0578	69.1859	0.7192	68.79	4.6546	0.7525
M-ARB	298	136.81	2.9839	0.9716	0.0503	111.4137	0.6477	110.38	6.5314	0.6769
	308	142.81	4.6229	0.9719	0.0539	115.8897	0.7609	115.29	7.1771	0.7871
	318	152.72	6.7535	0.9604	0.0566	123.5513	0.7604	123.30	7.9705	0.7904

In addition, the magnitude of the separation factor R_L can be calculated from $(1 + K_L C_0)^{-1}$ to determine whether the adsorption is beneficial. When the value of R_L is 0, the adsorption process can be considered irreversible. When the R_L value is 1, it can be judged that the adsorption is linear. When the R_L value is 0–1, the adsorption can be judged as favorable. As the R_L value exceeds 1, the adsorption can be judged to be unfavorable [52]. In this study, the R_L values of ARB and M-ARB were 0.0015–0.01 and 0.001–0.0083, respectively, demonstrating that the MB adsorption process by both ARB and M-ARB was favorable, and the appropriate increase of the initial MB concentration was more favorable for promoting the adsorption.

3.5. Adsorption Thermodynamics

The thermodynamic fitting results of the adsorption process of ARB and M-ARB on MB can be seen in Figure 10, and the fitted parameters depicted in Table 5. The ΔG^{θ}

values of ARB and M-ARB at different temperatures were negative and decreased with raising reaction temperature, demonstrating that the adsorption of these two-areca residue biochar on MB was spontaneous, and as the reaction temperature rose, this spontaneity grew [53]. The absolute value of ΔG^{θ} for M-ARB was greater than that for ARB at the same reaction temperature. It is, thus, clear that the spontaneous adsorption of MB through the NaOH-modified areca residue biochar was enhanced, and the modification could promote the spontaneous proceeding of the adsorption reaction, thus improving its adsorption performance on MB. Based on the fact that the value of ΔH^{θ} was greater than 0, it is known that the adsorption process of both ARB and M-ARB on MB was a heat absorption reaction [54]. The adsorption of MB by M-ARB required more heat for the reaction, so raising the reaction temperature can boost its ability to progress in a good way. The main types of adsorption reactions can be determined based on the magnitude of ΔH^{θ} values. When the value of ΔH^{θ} is less than 20 kJ/mol, the main form of adsorption could be considered physical adsorption. When the value of ΔH^{θ} is 20 to 80 kJ/mol, the main type of adsorption can be considered chemisorption [55]. In this study, the ΔH^{θ} values of ARB and M-ARB exceeded 20 kJ/mol, which indicated that their main reaction type for MB removal from water was chemisorption. The ΔH^{θ} value of M-ARB was 1.44 times higher than that of ARB, which indicated that chemisorption was more dominant in the removal of MB by M-ARB, which confirmed the results obtained from the previous adsorption kinetic analysis.

Table 5. Adsorption thermodynamic parameters of MB onto ARB and M-ARB.

T (K)	ΔG^{θ} (kJ/mol)		ΔH^{θ} (kJ/mol)		ΔS^{θ} [kJ/(mol × K)]		R^2	
	ARB	**M-ARB**	**ARB**	**M-ARB**	**ARB**	**M-ARB**	**ARB**	**M-ARB**
298	−8.5827	−10.2628						
308	−9.9041	−12.2349	38.9489	56.2585	0.1592	0.2229	0.9809	0.9937
318	−11.7668	−14.6803						

Additionally, the positive value of ΔS^{θ} indicated that the adsorption process of MB by both ARB and M-ARB was driven by entropy. The greater instability between the solid–liquid phases during the reaction improved the randomness of the reaction between MB molecules and active sites at the solid–liquid interface, and the greater disorder between the solid–liquid phases after the modification treatment was more favorable for the adsorption process [56].

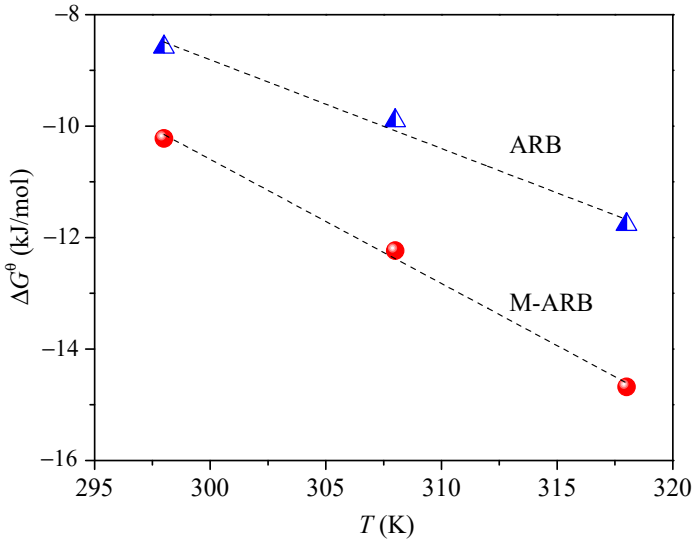

Figure 10. Adsorption thermodynamic fitting of MB onto ARB and M-ARB.

3.6. BET Analysis before and after Adsorption

Table 6 compares the changes of BET of ARB and M-ARB before and after adsorption of MB. As can be seen from Table 6, the specific surface area and total pore volume of ARB decreased by 68.25% and 71.34%, respectively, compared with those before the adsorption of MB. The specific surface area and total pore volume of M-ARB decreased 70.48% and 81.21%, respectively, compared with those before the adsorption of MB. While their average pore diameters increased 2.33 and 5.95 times, respectively, compared with those before the adsorption of MB. It demonstrated that the specific surface area and total pore volume of both areca residue biochar decreased significantly after the adsorption of MB, while the average pore size raised. It might because the decrease in the specific surface area and total pore volume because of the filling of pores on the biochar with MB after the adsorption reaction and the decrease in the number of mesopores and micropores due to the filling, thus increasing the average pore size. It was concluded that pore filling during adsorption was an important mechanism of action for the adsorption of MB by ARB and M-ARB. The role of pore filling in the adsorption of pollutants by biochar has been widely reported [57–59]. Moreover, from the comparison of the data, it can be found that the decrease in the specific surface area and total pore volume and the increase in average pore size of M-ARB were more obvious than those of ARB, showed that the pore filling was more intense during adsorption of MB by M-ARB, and more specific surface area and pores were utilized; thus, a higher amount of pollutants can be adsorbed, which became an important reason why the adsorption effect of M-ARB on MB was better than that of ARB. This is one of the important reasons why M-ARB had a better adsorption effect on MB than ARB.

Table 6. Comparison of BET analysis results before and after adsorption of MB.

Stage	Specific Surface Area (m^2/g)		Total Hole Volume (cm^3/g)		Average Pore Size (nm)	
	ARB	M-ARB	ARB	M-ARB	ARB	M-ARB
Before MB adsorption	63	105	0.157	0.282	5.593	3.416
After MB adsorption	20	31	0.045	0.053	18.611	20.325

3.7. FTIR Comparison before and after Adsorption

ARB and M-ARB surface functional group alterations prior to and during MB adsorption are depicted in Figure 11. It is evident that the surface of the areca residue biochar prepared by pyrolysis at 600 °C contained abundant functional group types. Among them, the ARB had stretching vibration peaks of -OH at 3431 cm^{-1}, C-H at 2926 cm^{-1}, and 2858 cm^{-1}, C=C and C=O at 1633 cm^{-1}, C-C at 1400 cm^{-1}, C-O at 1223 cm^{-1}, and the bending vibration peaks of Si-O-Si at 1105 cm^{-1} and 1034 cm^{-1} [60,61]. M-ARB had the stretching vibration peaks of -OH at 3427 cm^{-1}, C-H at 2918 cm^{-1}, and 2860 cm^{-1}, C=C and C=O at 1595 cm^{-1}, C-C at 1400 cm^{-1}, C-O at 1271 cm^{-1}, and the bending vibration peaks of Si-O-Si at 1099 cm^{-1} and 1026 cm^{-1} and C-H at 796 cm^{-1} [62]. Except for the absorption peak position of C-C, which was the same, after NaOH treatment, the locations of the remaining functional groups' absorption peaks were altered, with the most obvious shift of the absorption peaks at C=O and C=C, and a new C-H bending vibration peak was also generated. This showed that the NaOH modification could change the surface functional group structure of biochar and bring more functional group types to biochar. It was analyzed that NaOH modification could open the pores on biochar that were originally blocked, and at the same time, dissolve some substances on the surface of biochar that masked the functional groups, thus allowing for better exposure of the functional groups, which could provide favorable conditions for the better adsorption of pollutants by areca residue biochar [63].

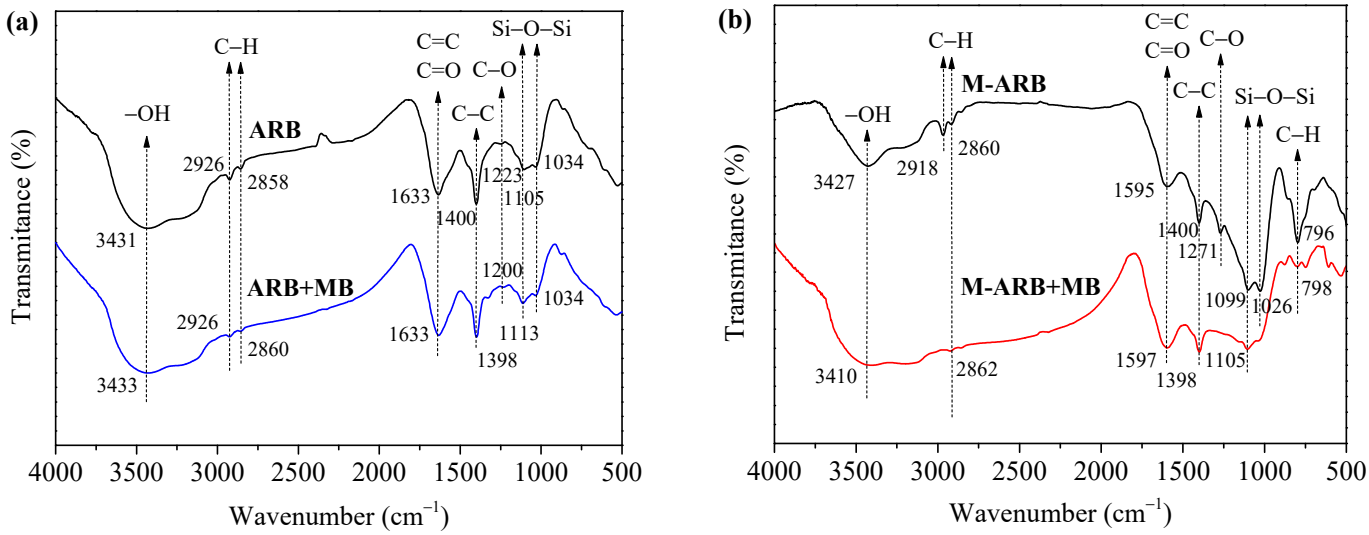

Figure 11. FTIR spectra of ARB (**a**) and M-ARB (**b**) before and after MB adsorption.

The locations of the absorbance peak of several functional groups of ARB and M-ARB were changed to varying degrees after MB had been absorbed. Among them, the -OH absorption peaks of ARB and M-ARB were shifted to 3433 cm^{-1} and 3410 cm^{-1}, respectively. This has to do with the creation of hydrogen bonds between the biochar's -OH and the heterocycles on MB that contain nitrogen; thus, hydrogen bonding had a significant impact on the adsorption [64,65]. The C-H stretching vibration peak of ARB at 2858 cm^{-1} had been changed to 2860 cm^{-1}, while the peak at 2926 cm^{-1} had not. The C-H stretching vibration peak of M-ARB at 2860 cm^{-1} was displaced to 2862 cm^{-1}, while the peak at 2918 cm^{-1} vanished. The C=O and C=C absorption peaks of ARB remained in their original locations, whereas M-ARB's C=O and C=C absorption peaks changed to 1597 cm^{-1}, implying the presence of π–π bonding between MB and NaOH-modified areca residue biochar [66]. However, this effect was weaker in the unmodified areca residue biochar and was not sufficient to change its absorption peak position. The C-C absorption peaks of both ARB and M-ARB were shifted to 1398 cm^{-1}, indicating the involvement of C-C functional groups in the adsorption reaction. The C-O absorption peak of ARB moved to 1200 cm^{-1}, while that of M-ARB disappeared. The Si-O-Si bending vibration peak of ARB at 1105 cm^{-1} moved to 1113 cm^{-1}, while the peak at 1034 cm^{-1} was not offset. The Si-O-Si bending vibration peak of M-ARB at 1099 cm^{-1} shifted to 1105 cm^{-1}, while the peak at 1026 cm^{-1} disappeared. In addition, following the adsorption of MB, the newly formed C-H bending vibration peak of M-ARB changed to 798 cm^{-1}, demonstrating that C-H was also engaged in the adsorption reaction. This showed that the NaOH-modified areca residue biochar not only had a richer surface functional group structure, but also the type of functional groups involved in the adsorption reaction and the degree of participation had been enhanced, which enabled it to show better MB removal during adsorption [67].

The adsorption mechanism of ARB and M-ARB for MB in water is depicted in Figure 12.

As can be seen from Figure 12, the adsorption mechanism of ARB on MB mainly involved electrostatic gravitational force, pore filling, and hydrogen bonding, while the adsorption mechanism of M-ARB on MB also involved π–π bonding and the combined effect of other types of functional groups. The adsorption of MB by ARB and M-ARB was a complex process with multiple mechanisms. Wang et al. [68] prepared HNO_3-activated and tannic acid-enhanced reed biochar as an adsorbent for MB and showed that the adsorption process was closely related to electrostatic interactions, hydrogen bonding, ion exchange, and n–π/π–π interactions. Zhang et al. [69] prepared biochar from hickory chip and obtained modified biochar for MB adsorption using ball milling and H_2O_2 treatment. The mechanism involved in this adsorption process includes π–π and van der

Waals attraction mechanism, electrostatic interaction, and ion exchange. Wang et al. [70] used K_2CO_3 modified waste bamboo biochar to remove MB from water, and it was found that electrostatic attraction, hydrogen bonding, and π–π interactions all contributed to MB adsorption. All these studies generally confirmed that the adsorption of MB by biochar was not a single adsorption mechanism, similar to the conclusion obtained in this study. The NaOH modification gave the areca residue biochar a better and more complex structure, thus giving it a greater adsorption potential and creating a valuable and optional pathway for the removal of MB.

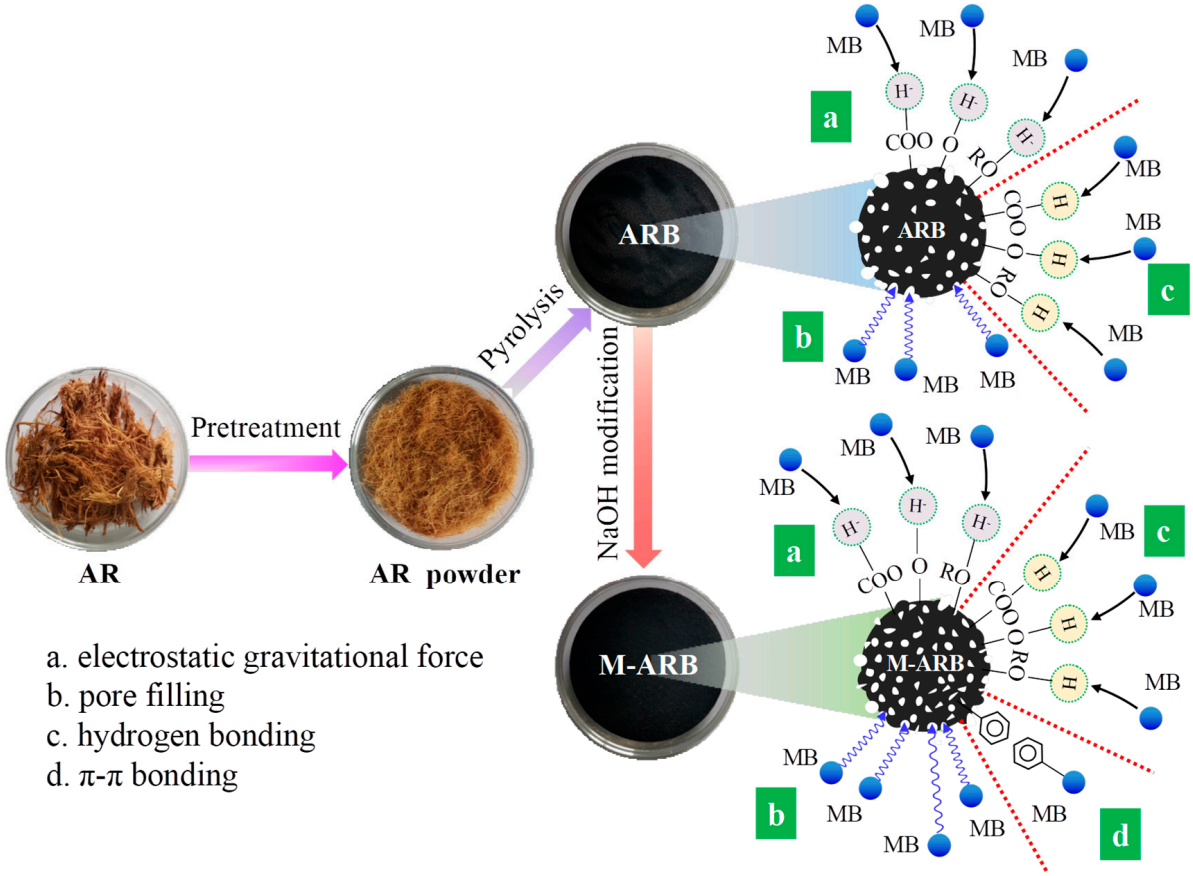

Figure 12. Adsorption mechanism of ARB and M-ARB for MB.

3.8. Analysis of Regeneration Performance

Figure 13 shows the change of MB removal rate of ARB and M-ARB after five times of regeneration. It can be seen that, with the increase of adsorption-desorption times, the removal rates of MB by ARB and M-ARB showed a downward trend, and the downward trend of ARB was more obvious. After recycling twice, the removal rate of MB by M-ARB was still above 90%. After five times of recycling, the removal rate of MB by M-ARB decreased significantly, but still reached 85.86%, showing good reusability. The removal rate of MB by ARB had dropped to 69.21% by the fifth time of recycling, 16.65 percentage points lower than that of MB by M-ARB. Accordingly, the regeneration performance of areca residue biochar without NaOH modification was relatively poor. NaOH modification enabled areca residue biochar to have a more perfect structure and better physical and chemical properties, so it can still have a higher pollutant removal efficiency after multiple recycling and show better economic and environmental benefits in practical application.

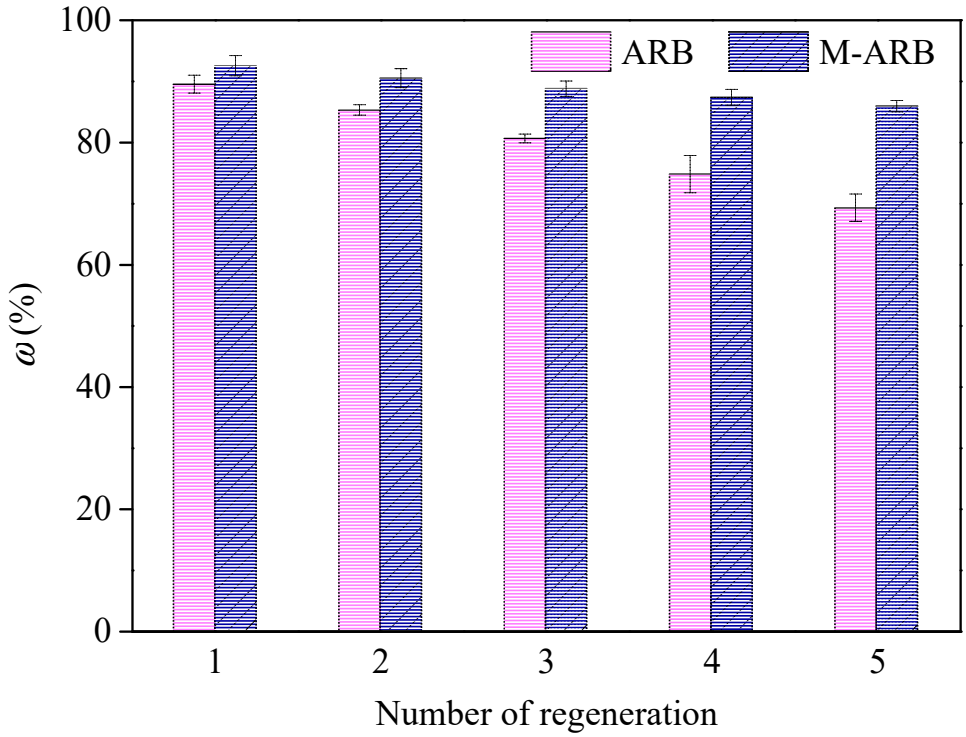

Figure 13. Regeneration performance of ARB and M-ARB for MB adsorption.

3.9. Comparison of Adsorption Capacity

Table 7 lists the adsorption capacity of several biochars for MB in water. It can be seen that, due to the different raw materials and modification methods of biochars, their adsorption capacity for MB also varies greatly. In contrast, under relatively simple preparation and modification conditions, M-ARB in this study, reached a higher MB adsorption capacity in a relatively short contact time, which has great potential to become a high-quality MB adsorbent. The preparation of NaOH modified biochar from areca residue for MB treatment showed good applicability in wastewater treatment and solid waste reuse and helped to promote sustainable ecological development.

Table 7. Comparison of adsorption capacity of different biochar materials for MB.

Raw Materials	Modifying Agent	Pyrolysis Temperature (°C)	Pyrolysis Time (min)	Contact Time (min)	Adsorption Capacity (mg/g)	References
Tea residue	NaOH	700	240	150	105.44	[28]
Reed	HNO_3	500	120	720	37.18	[68]
Tea residue	KOH+$FeCl_3$	700	120	360	394.30	[71]
Lychee seed	KOH	700	—	300	124.53	[72]
Lasia rhizome	None	300	180	—	9.58	[73]
Lasia rhizome	HNO_3	300	180	—	81.35	[73]
Fallen leaf	None	500	120	1440	78.60	[74]
Cotton residue	None	550	15	720	9.56	[75]
Cotton residue	NaOH	550	15	720	23.82	[75]
Sewage sludge	None	600	60	—	51.10	[76]
ARB	None	600	150	400	86.56	This study
M-ARB	NaOH	600	150	400	152.72	This study

4. Conclusions

This research examined the viability, influencing factors, and mechanisms of adsorption of MB in water via ARB and M-ARB. NaOH modification not only dramatically raised the specific surface area and total pore volume of ARB, but also increased its oxygen content, and enabled it to possess a richer type of surface functional groups and exhibit greater adsorption potential. The theoretical maximum adsorption of MB in water by M-ARB ranged from 136.81 mg/g to 152.72 mg/g, which was increased by 74.99–76.59%, compared with that before modification. The mechanism involved in the adsorption process of M-ARB for MB was more abundant, including the electrostatic gravitational force, pore filling, hydrogen bonding, and π–π bonding, which was a complex process. The conversion of waste areca residue into biochar that can effectively adsorb MB in water provided a preferred pathway for the removal of MB and also provided a new strategy to effectively solve the environmental pollution problems caused by areca residue.

Author Contributions: Conceptualization, Y.L. (Yixin Lu) and C.W.; data curation, Y.L. (Yujie Liu); formal analysis, C.L.; funding acquisition, Y.L. (Yixin Lu) and C.W.; methodology, Y.T.; supervision, C.W.; visualization, A.W.; writing—original draft, H.L. (Haolin Liu) and H.L. (Huan Liu); writing—review and editing, C.T. All authors have read and agreed to the published version of the manuscript.

Funding: This research was funded by the Natural Science Foundation of Sichuan Province (2022NSFSC0393), Sichuan Science and Technology Program (2022YFG0307), National College Students' Innovation Training Program (202211116025), University's Scientific Research Project of CDTU (2022ZR001), Laboratory Open Fund Project of CDTU (2022CHZH04), and Transverse Project ((2022)82), ((2022)130).

Institutional Review Board Statement: Not applicable.

Informed Consent Statement: Not applicable.

Data Availability Statement: Data are contained within the article.

Conflicts of Interest: The authors declare no conflict of interest.

References

1. Huang, H.; Wang, T.; Han, S.; Bai, Y.; Li, X.Q. Occurrence of areca alkaloids in wastewater of major Chinese cities. *Sci. Total Environ.* **2021**, *783*, 146961. [CrossRef] [PubMed]
2. Subramani, B.; Sheeka, S.S.; Manu, B.; Babunarayan, K.S. Evaluation of pyrolyzed areca husk as a potential adsorbent for the removal of Fe^{2+} ions from aqueous solutions. *J. Environ. Manag.* **2019**, *246*, 345–354. [CrossRef] [PubMed]
3. Rahali, A.; Riazi, A.; Moussaoui, B.; Boucherdoud, A.; Bekta, N. Decolourisation of methylene blue and congo red dye solutions by adsorption using chitosan. Desalin. *Water Treat.* **2020**, *198*, 422–433.
4. Siciliano, A.; Curcio, G.M.; Limonti, C.; Masi, S.; Greco, M. Methylene blue adsorption on thermo plasma expanded graphite in a multilayer column system. *J. Environ. Manag.* **2021**, *296*, 113365. [CrossRef] [PubMed]
5. Ghodbane, I.Z.; Saida, L.; Rim, K.; Rochdi, K. Development of new modified electrode based on beta-cyclodextrin for methylene blue detection. *Sens. Rev.* **2020**, *40*, 477–483. [CrossRef]
6. Punnakkal, V.S.; Jos, B.; Anila, E.I. Polypyrrole-silver nanocomposite for enhanced photocatalytic degradation of methylene blue under sunlight irradiation. *Mater. Lett.* **2021**, *298*, 130014. [CrossRef]
7. Giraldo, S.; Robles, I.; Godínez, L.; Acelas, N.; Flórez, E. Experimental and theoretical insights on methylene blue removal from wastewater using an adsorbent obtained from the residues of the orange industry. *Molecules* **2021**, *26*, 4555. [CrossRef]
8. Perez-Gonzalez, M.; Tomas, S.A. Surface chemistry of TiO_2-ZnO thin films doped with Ag. Its role on the photocatalytic degradation of methylene blue. *Catal. Today* **2021**, *360*, 129–137. [CrossRef]
9. Nwanebu, E.O.; Liu, X.; Pajootan, E.; Yargeau, V.; Omanovic, S. Electrochemical degradation of methylene blue using a Ni-Co-Oxide anode. *Catalysts* **2021**, *11*, 793. [CrossRef]
10. Balushi, K.S.; Devi, G.; Hudaifi, A.; Garibi, A.S.R. Development of chitosan-TiO_2 thin film and its application for methylene blue dye degradation. *Int. J. Environ. Anal. Chem.* **2021**, *2*, 1–14. [CrossRef]
11. Eren, Z.; O'Shea, K. Hydroxyl radical generation and partitioning in degradation of methylene blue and DEET by dual-frequency ultrasonic irradiation. *J. Envior. Eng.* **2019**, *145*, 04019070. [CrossRef]
12. Pan, J.; Zhou, L.; Chen, H.; Liu, X.; Hong, C.; Chen, D.; Pan, B. Mechanistically understanding adsorption of methyl orange, indigo carmine, and methylene blue onto ionic/nonionic polystyrene adsorbents. *J. Hazard. Mater.* **2021**, *418*, 126300. [CrossRef]
13. Mittal, J.; Arora, C.; Mittal, A. Application of biochar for the removal of methylene blue from aquatic environments. In *Biomass-Derived Materials for Environmental Applications*; Elsevier: Amsterdam, The Netherlands, 2022; pp. 29–76.

14. Viegas, C.; Nobre, C.; Correia, R.; Gouveia, L.; Goncalves, M. Optimization of biochar production by co-torrefaction of microalgae and lignocellulosic biomass using response surface methodology. *Energies* **2021**, *14*, 7330. [CrossRef]
15. Prabakaran, E.; Pillay, K.; Brink, H. Hydrothermal synthesis of magnetic-biochar nanocomposite derived from avocado peel and its performance as an adsorbent for the removal of methylene blue from wastewater. *Mater. Today Sustain.* **2022**, *18*, 100123. [CrossRef]
16. Prajapati, A.K.; Mondal, M.K. Green synthesis of Fe_3O_4-onion peel biochar nanocomposites for adsorption of Cr(VI), methylene blue and congo red dye from aqueous solutions. *J. Mol. Liq.* **2022**, *349*, 118161. [CrossRef]
17. Zhu, Y.; Yi, B.; Hu, H.; Zong, Z.; Chen, M.; Yuan, Q. The relationship of structure and organic matter adsorption characteristics by magnetic cattle manure biochar prepared at different pyrolysis temperatures. *J. Environ. Chem. Eng.* **2020**, *8*, 104112. [CrossRef]
18. Yin, Q.; Nie, Y.; Han, Y.; Wang, R.; Zhao, Z. Properties and the application of sludge-based biochar in the removal of phosphate and methylene blue from water: Effects of acid treating. *Langmuir* **2022**, *38*, 1833–1844. [CrossRef]
19. Ezz, H.; Ibrahim, M.G.; Fujii, M.; Nasr, M. Enhanced removal of methylene blue dye by sustainable biochar derived from rice straw digestate. *Key Eng. Mater.* **2022**, *932*, 119–129. [CrossRef]
20. Chen, J.; Tang, C.; Li, X.; Sun, J.; Liu, Y.; Huang, W.; Wang, A.; Lu, Y. Preparation and modification of rape straw biochar and its adsorption characteristics for methylene blue in water. *Water* **2022**, *14*, 3761. [CrossRef]
21. Sawalha, H.; Bader, A.; Sarsour, J.; Al-Jabari, M.; Rene, E.R. Removal of dye (methylene blue) from wastewater using bio-char derived from agricultural residues in palestine: Performance and isotherm analysis. *Processes* **2022**, *10*, 2039. [CrossRef]
22. Xie, Y.; Wang, L.; Li, H.; Westholm, L.J.; Carvalho, L.; Thorin, E.; Yu, Z.; Yu, X.; Skreiberg, O. A critical review on production, modification and utilization of biochar. *J. Anal. Appl. Pyrolysis* **2022**, *161*, 105405. [CrossRef]
23. Zhang, Q.; Wang, J.; Lyu, H.; Zhao, Q.; Lisi, J.; Li, L. Ball-milled biochar for galaxolide removal: Sorption performance and governing mechanisms. *J. Clin. Microbiol.* **2019**, *659*, 1537–1545. [CrossRef] [PubMed]
24. Kwak, J.H.; Islam, M.S.; Wang, S.; Messele, S.A.; Naeth, M.A.; El-Din, M.G.; Chang, S.X. Biochar properties and lead(II) adsorption capacity depend on feedstock type, pyrolysis temperature, and steam activation. *Chemosphere* **2019**, *231*, 393–404. [CrossRef] [PubMed]
25. Miao, Q.; Li, G. Potassium phosphate/magnesium oxide modified biochars: Interfacial chemical behaviours and Pb binding performance. *J. Clin. Microbiol.* **2021**, *759*, 143452. [CrossRef]
26. Zhang, S.; Wang, J. Removal of chlortetracycline from water by immobilized Bacillus subtilis on honeysuckle residue derived biochar. *Water Air Soil Pollut.* **2021**, *232*, 236. [CrossRef]
27. Hussin, M.H.; Chuein, A.L.H.; Idris, N.N.; Hamidon, T.S.; Azani, N.F.S.M.; Abdullah, N.S.; Sharifuddin, S.S.; Ying, A.S. Kinetics and equilibrium studies of methylene blue dye adsorption on oil palm frond adsorbent. *Desalin. Water Treat.* **2021**, *216*, 358–371.
28. Mu, Y.; Ma, H. NaOH-modified mesoporous biochar derived from tea residue for methylene blue and Orange II removal. *Chem. Eng. Res. Des.* **2021**, *167*, 129–140. [CrossRef]
29. Choudhary, M.; Kumar, R.; Neogi, S. Activated biochar derived from *Opuntia ficus-indica* for the efficient adsorption of malachite green dye, Cu^{+2} and Ni^{+2} from water. *J. Hazard. Mater.* **2020**, *392*, 122441. [CrossRef]
30. Zhou, Y.; Li, Z.; Ji, L.; Wang, Z.; Cai, L.; Guo, J.; Song, W.; Wang, Y.; Piotrowski, A.M. Facile preparation of alveolate biochar derived from seaweed biomass with potential removal performance for cationic dye. *J. Mol. Liq.* **2022**, *353*, 118623. [CrossRef]
31. Vu, M.T.; Le, T.T.; Chao, H.P.; Trinh, T.V.; Lin, C.C.; Tran, H.N. Removal of ammonium from groundwater using NaOH-treated activated carbon derived from corncob wastes: Batch and column experiments. *J. Clean. Prod.* **2018**, *180*, 560–570. [CrossRef]
32. Boguta, P.; Sokolowska, Z.; Skic, K.; Tomczyk, A. Chemically engineered biochar-Effect of concentration and type of modifier on sorption and structural properties of biochar from wood waste. *Fuel* **2019**, *256*, 115893. [CrossRef]
33. Lu, F.; Lu, X.; Li, S.; Zhang, H.; Shao, L.; He, P. Dozens-fold improvement of biochar redox properties by KOH activation. *Chem. Eng. J.* **2022**, *429*, 132203. [CrossRef]
34. Wu, J.; Wang, L.; Ma, H.; Zhou, J. Investigation of element migration characteristics and product properties during biomass pyrolysis: A case study of pine cones rich in nitrogen. *RSC Adv.* **2021**, *11*, 34795–34805. [CrossRef]
35. Cai, T.; Du, H.; Liu, X.; Tie, B.; Zeng, Z. Insights into the removal of Cd and Pb from aqueous solutions by NaOH-EtOH-modified biochar. *Environ. Technol. Innov.* **2021**, *24*, 102031. [CrossRef]
36. Huang, M.; Liao, Z.; Li, Z.; Wen, J.; Zhao, L.; Jin, C.; Tian, D.; Shen, F. Effects of pyrolysis temperature on proton and cadmium binding properties onto biochar-derived dissolved organic matter: Roles of fluorophore and chromophore. *Chemosphere* **2022**, *299*, 134313. [CrossRef]
37. Li, X.; Jiang, X.; Song, Y.; Chang, S. Coexistence of polyethylene microplastics and biochar increases ammonium sorption in an aqueous solution. *J. Hazard. Mater.* **2020**, *405*, 124260. [CrossRef]
38. Ahmad, A.; Khan, N.; Giri, B.S.; Chaturvedi, P.; Chowdhary, P. Removal of methylene blue dye using rice husk, cow dung and sludge biochar: Characterization, application, and kinetic studies. *Bioresour. Technol.* **2020**, *306*, 123202. [CrossRef]
39. Feng, Q.; Chen, M.; Wu, P.; Zhang, X.; Wang, S.; Yu, Z.; Wang, B. Simultaneous reclaiming phosphate and ammonium from aqueous solutions by calcium alginate-biochar composite: Sorption performance and governing mechanisms. *Chem. Eng. J.* **2022**, *429*, 132166. [CrossRef]
40. Wang, B.; Lian, G.; Lee, X.; Gao, B.; Li, L.; Liu, T.; Zhang, X.; Zheng, Y. Phosphogypsum as a novel modifier for distillers grains biochar removal of phosphate from water. *Chemosphere* **2020**, *38*, 124684. [CrossRef] [PubMed]

41. Zhou, H.; Ye, M.; Zhao, Y.; Baig, S.A.; Huang, N.; Ma, M. Sodium citrate and biochar synergistic improvement of nanoscale zero-valent iron composite for the removal of chromium (VI) in aqueous solutions. *J. Environ. Sci.* **2022**, *115*, 227–239. [CrossRef] [PubMed]
42. Akech, S.R.O.; Harrison, O.; Saha, A. Removal of a potentially hazardous chemical, tetrakis (hydroxymethyl) phosphonium chloride from water using biochar as a medium of adsorption. *Environ. Technol. Innov.* **2018**, *12*, 196–210. [CrossRef]
43. Ramola, S.; Belwal, T.; Li, C.; Liu, Y.; Wang, Y.; Yang, S.; Zhou, C. Preparation and application of novel rice husk biochar-calcite composites for phosphate removal from aqueous medium. *J. Clean. Prod.* **2021**, *299*, 126802. [CrossRef]
44. Olu-Owolabi, B.I.; Diagboya, P.N.; Mtunzi, F.M.; During, R.A. Utilizing eco-friendly kaolinite-biochar composite adsorbent for removal of ivermectin in aqueous media. *J. Environ. Manag.* **2021**, *279*, 111619. [CrossRef]
45. Saikia, R.; Goswami, R.; Bordoloi, N.; Senapati, K.K.; Pant, K.K.; Kumar, M.; Kataki, R. Removal of arsenic and fluoride from aqueous solution by biomass based activated biochar: Optimization through response surface methodology. *J. Environ. Chem. Eng.* **2017**, *5*, 5528–5539. [CrossRef]
46. An, Q.; Li, Z.; Zhou, Y.; Meng, F.; Zhao, B.; Miao, Y.; Deng, S. Ammonium removal from groundwater using peanut shell based modified biochar: Mechanism analysis and column experiments. *J. Water Process Eng.* **2021**, *43*, 102219. [CrossRef]
47. Kaith, B.S.; Shanker, U.; Gupta, B. Synergic effect of Guggul gum based hydrogel nanocomposite: An approach towards adsorption-photocatalysis of Magenta-O. *Int. J. Biol. Macromol.* **2020**, *161*, 457–469. [CrossRef]
48. Qing, Z.; Wang, L.; Liu, X.; Song, Z.; Qian, F.; Song, Y. Simply synthesized sodium alginate/zirconium hydrogel as adsorbent for phosphate adsorption from aqueous solution: Performance and mechanisms. *Chemosphere* **2022**, *291*, 133103. [CrossRef]
49. Qiao, H.; Qiao, Y.; Luo, X.; Zhao, B.; Cai, Q. Qualitative and quantitative adsorption mechanisms of zinc ions from aqueous solutions onto dead carp derived biochar. *RSC Adv.* **2021**, *11*, 38273–38282. [CrossRef]
50. Yang, Z.; Hu, W.; Yao, B.; Shen, L.; Jiang, F.; Zhou, Y.; Nunez-Delgado, A. A novel manganese-rich pokeweed biochar for highly efficient adsorption of heavy metals from wastewater: Performance, mechanisms, and potential risk analysis. *Processes* **2021**, *9*, 1209. [CrossRef]
51. Li, S.B.; Dong, L.J.; Wei, Z.F.; Sheng, G.D.; Du, K.; Hu, B.W. Adsorption and mechanistic study of the invasive plant-derived biochar functionalized with CaAl-LDH for Eu(III) in water. *J. Environ. Sci.* **2020**, *96*, 127–137. [CrossRef]
52. Shen, Y.W.; Jiao, S.Y.; Ma, Z.; Gao, W.S.; Chen, J.Q. Humic acid-modified bentonite composite material enhances urea-nitrogen use efficiency. *Chemosphere* **2020**, *255*, 126976. [CrossRef] [PubMed]
53. Liu, Z.F.; Fang, X.; Chen, L.Y.; Tang, B.; Song, F.M.; Li, W.B. Effect of acid-base modified biochar on chlortetracycline adsorption by purple soil. *Sustainability* **2022**, *14*, 5892. [CrossRef]
54. Kaya-Zkiper, K.; Uzun, A.; Soyer-Uzun, S. A novel alkali activated magnesium silicate as an effective and mechanically strong adsorbent for methylene blue removal. *J. Hazard. Mater.* **2022**, *424*, 127256. [CrossRef] [PubMed]
55. Lu, Y.X.; Chen, J.; Zhao, L.; Zhou, Z.; Qiu, C.; Li, Q.L. Adsorption of Rhodamine B from aqueous solution by goat manure biochar: Kinetics, isotherms, and thermodynamic studies. *Pol. J. Environ. Stud.* **2020**, *2*, 2721–2730. [CrossRef] [PubMed]
56. Yan, Y.H.; Chu, Y.T.; Khan, M.A.; Xia, M.Z.; Shi, M.X.; Zhu, S.D.; Lei, W.; Wang, F.Y. Facile immobilization of ethylenediamine tetramethylene-phosphonic acid into UiO-66 for toxic divalent heavy metal ions removal: An experimental and theoretical exploration. *Sci. Total Environ.* **2022**, *806*, 150652. [CrossRef]
57. Cheng, D.L.; Ngo, H.H.; Guo, W.S.; Chang, S.W.; Nguyen, D.D.; Li, J.X.; Ly, Q.V.; Nguyen, T.A.H.; Tran, V.S. Applying a new pomelo peel derived biochar in microbial fell cell for enhancing sulfonamide antibiotics removal in swine wastewater. *Bioresour. Technol.* **2020**, *318*, 123886. [CrossRef]
58. Gao, T.; Shi, W.S.; Zhao, M.X.; Huang, Z.X.; Liu, X.L.; Ruan, W.Q. Preparation of spiramycin fermentation residue derived biochar for effective adsorption of spiramycin from wastewater. *Chemosphere* **2022**, *296*, 133902. [CrossRef]
59. Li, Y.X.; Shang, H.R.; Cao, Y.N.; Yang, C.H.; Feng, Y.J.; Yu, Y.L. High performance removal of sulfamethoxazole using large specific area of biochar derived from corncob xylose residue. *Biochar* **2022**, *1*, 151–161. [CrossRef]
60. Yang, X.D.; Wang, L.L.; Tong, J.; Shao, X.Q.; Chen, R.; Yang, Q.; Li, F.F.; Xue, B.; Li, G.D.; Han, Y.; et al. Synthesis of hickory biochar via one-step acidic ball milling: Characteristics and titan yellow adsorption. *J. Clean. Prod.* **2022**, *338*, 130575. [CrossRef]
61. Wang, T.T.; Zhang, D.; Fang, K.K.; Zhu, W.; Peng, Q.; Xie, Z.G. Enhanced nitrate removal by physical activation and Mg/Al layered double hydroxide modified biochar derived from wood waste: Adsorption characteristics and mechanisms. *J. Environ. Chem. Eng.* **2021**, *9*, 105184. [CrossRef]
62. Zhang, Y.; Tang, J.Y.; Zhang, W.J.; Ai, J.; Liu, Y.Y.; Wang, Q.D.; Wang, D.S. Preparation of ultrahigh-surface-area sludge biopolymers-based carbon using alkali treatment for organic matters recovery coupled to catalytic pyrolysis. *J. Environ. Sci.* **2021**, *106*, 83–96. [CrossRef]
63. Chen, W.; Gong, M.; Li, K.X.; Xia, M.W.; Chen, Z.Q.; Xiao, H.Y.; Fang, Y.; Chen, Y.Q.; Yang, H.P.; Chen, H.P. Insight into KOH activation mechanism during biomass pyrolysis: Chemical reactions between O-containing groups and KOH. *Appl. Energy* **2020**, *278*, 115730. [CrossRef]
64. Hu, M.F.; Liu, L.; Hou, N.; Li, X.S.; Zeng, D.Q.; Tan, H.H. Insight into the adsorption mechanisms of ionizable imidazolinone herbicides in sediments: Kinetics, adsorption model, and influencing factors. *Chemosphere* **2021**, *274*, 129655. [CrossRef]
65. Binh, Q.A.; Kajitvichyanukul, P. Adsorption mechanism of dichlorvos onto coconut fibre biochar: The significant dependence of H-bonding and the pore-filling mechanism. *Water Sci. Technol.* **2019**, *79*, 866–876. [CrossRef]

66. Deng, H.; Zhang, J.Y.; Huang, R.; Wang, W.; Meng, M.W.; Hu, L.N.; Gan, W.X. Adsorption of malachite green and Pb^{2+} by $KMnO_4$-modified biochar: Insights and mechanisms. *Sustainability* **2022**, *14*, 2040. [CrossRef]
67. Zheng, Y.W.; Wang, J.D.; Li, D.H.; Liu, C.; Lu, Y.; Lin, X.; Zheng, Z.F. Insight into the $KOH/KMnO_4$ activation mechanism of oxygen-enriched hierarchical porous biochar derived from biomass waste by in-situ pyrolysis for methylene blue enhanced adsorption. *J. Anal. Appl. Pyrolysis* **2021**, *158*, 105269. [CrossRef]
68. Wang, Y.; Zhang, Y.; Li, S.Y.; Zhong, W.H.; Wei, W. Enhanced methylene blue adsorption onto activated reed-derived biochar by tannic acid. *J. Mol. Liq.* **2018**, *268*, 658–666. [CrossRef]
69. Zhang, Y.; Zheng, Y.L.; Yang, Y.C.; Huang, J.S.; Zimmerman, A.R.; Chen, H.; Hu, X.; Gao, B. Mechanisms and adsorption capacities of hydrogen peroxide modified ball milled biochar for the removal of methylene blue from aqueous solutions. *Bioresour. Technol.* **2021**, *337*, 125432. [CrossRef]
70. Wang, Y.H.; Srinivasakannan, C.; Wang, H.H.; Xue, G.; Wang, L.; Wang, X.; Duan, X. Preparation of novel biochar containing graphene from waste bamboo with high methylene blue adsorption capacity. *Diam. Relat. Mater.* **2022**, *125*, 109034. [CrossRef]
71. Mu, Y.K.; Du, H.X.; He, W.Y.; Ma, H.Z. Functionalized mesoporous magnetic biochar for methylene blue removal: Performance assessment and mechanism exploration. *Diam. Relat. Mater.* **2022**, *121*, 108795. [CrossRef]
72. Sahu, S.; Pahi, S.; Tripathy, S.; Singh, S.K.; Behera, A.; Sahu, U.K.; Patal, R.K. Adsorption of methylene blue on chemically modified lychee seed biochar: Dynamic, equilibrium, and thermodynamic study. *J. Mol. Liq.* **2020**, *315*, 113743. [CrossRef]
73. Fernando, J.C.; Peiris, C.; Navarathna, C.M.; Gunatilake, S.R.; Welikala, U.; Wanasinghe, S.T.; Madduri, S.B.; Jayasinghe, S.; Mlsna, T.E.; Hassan, E.; et al. Nitric acid surface pre-modification of novel Lasia spinosa biochar for enhanced methylene blue remediation. *Groundw. Sustain. Dev.* **2021**, *14*, 100603. [CrossRef]
74. Ji, B.; Wang, J.L.; Song, H.J. Removal of methylene blue from aqueous solutions using biochar derived from a fallen leaf by slow pyrolysis: Behavior and mechanism. *J. Environ. Chem. Eng.* **2019**, *7*, 103036. [CrossRef]
75. Primaz, C.T.; Ribes-Greus, A.; Jacques, R.A. Valorization of cotton residues for production of bio-oil and engineered biochar. *Energy* **2021**, *235*, 121363. [CrossRef]
76. Ribeiro, M.R.; Guimarães, Y.D.; Silva, I.F.; Almeida, C.A.; Silva, M.S.V.; Nascimento, M.A.; da Silva, U.P.; Varejao, E.V.; Renato, N.D.; Teixeira, A.P.D.; et al. Synthesis of value-added materials from the sewage sludge of cosmetics industry effluent treatment plant. *J. Environ. Chem. Eng.* **2021**, *9*, 105367. [CrossRef]